

## The Orbital Determination Of 1999 GJ2 Using the Method of Gauss

CHEN, T., CHITNIS, A., KLEIMAN, S., SOONG, A.<sup>1</sup>

<sup>1</sup>*Summer Science Program and Sommers-Bausch Observatory, University of Colorado Boulder, Boulder, CO, 80309,  
USA*

(Received July 23, 2022)

### ABSTRACT

Asteroid orbit determination is vital for predicting potentially catastrophic collisions with Earth. The main focus of this paper is the orbital determination of the Near Earth Asteroid 1999 GJ2. Using data from three observations from a 20" f/6.8, reflecting PlaneWave telescope, the Method of Gauss was performed to calculate the asteroid's position and velocity, which were then used to calculate the classical orbital elements: semi-major axis ( $a$ ), eccentricity ( $e$ ), inclination ( $i$ ), longitude of ascending node ( $\Omega$ ), argument of perihelion ( $\omega$ ), and mean anomaly ( $M$ ). The time of last perihelion passage ( $T$ ) was also calculated. After running a 100,000 iteration Monte Carlo simulation, final values of  $a = 1.53473 \pm 0.00077 AU$ ,  $e = 0.19705 \pm 0.00046$ ,  $i = 11.29781 \pm 0.00413^\circ$ ,  $\Omega = 196.30890 \pm 0.04513^\circ$ ,  $\omega = 142.49775 \pm 0.00481^\circ$ ,  $M = 316.23192 \pm 0.07762^\circ$ , and  $T = 2459162.64815 \pm 0.60753 JD$  were found. These orbital elements were then used to generate an ephemeris that was compared to the third observation from July 14th, 2022 at 04:41:39.0250 (UTC). The percent error for the right ascension ( $\alpha$ ) was  $1.02446 \times 10^{-5}\%$  while the percent error for the asteroid's declination ( $\delta$ ) was  $6.75249 \times 10^{-5}\%$ .

## 1. INTRODUCTION

The solar system is full of different types of debris, ranging from comets to asteroids to man-made satellites. Comets, for instance, are remnants from the solar system's formation composed of dust, ice, and rock with highly eccentric orbits. They originate from the Kuiper belt which extends beyond Neptune's orbit, and they can occasionally be perturbed into the inner solar system by Jupiter (Barnett, 2019) (1). Asteroids, the focus of this study's orbital determination, are also results of the solar system's formation. The majority of asteroids composed of clay and silicate are often referred to as C-type asteroids; S-type asteroids are made of silicate materials and nickel-iron; M-type asteroids are metallic, usually composed of nickel-iron and reflect radar well due to their metallic composition (Barnett, 2021) (2). Asteroids are further classified based on their orbits: some asteroids, Trojan asteroids, are found along Jupiter's orbit with orbital periods around twelve years. On the other hand, asteroids are often found between the orbits of Earth and Jupiter in the Main Asteroid Belt, where their orbital periods fall between 3.3 to 6 years.

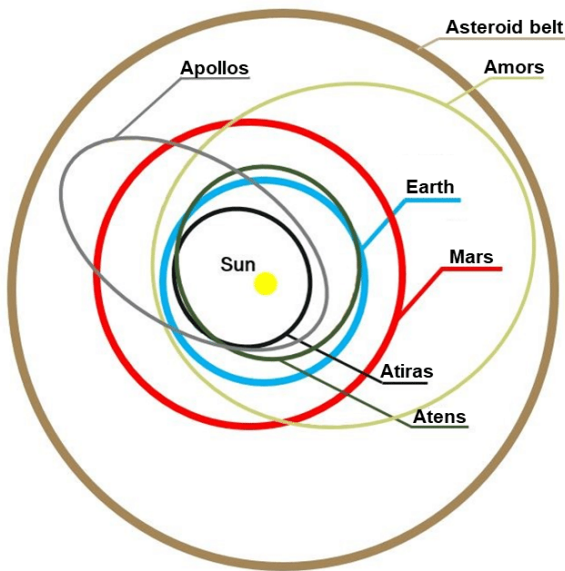


**Figure 1.** Illustration of the four main Near-Earth Asteroid groups according to their orbits in relation to the Sun, Earth's, and Mars' orbits and the Asteroid Belt. (Biktymiroy 2019) (11)

A specific category of these asteroids are called “Near Earth Asteroids” (NEAs). NEAs have a perihelion of less than 1.3 astronomical units and can be placed into subcategories based on their orbits. Figure 1 depicts the main NEA asteroid groups. Out of the 29,231 NEAs discovered (NASA JPL Center for Near Earth Object Studies 2022)(3) , only about 0.1% of them are a part of the Atira group, a group of asteroids that have an aphelion of less than one AU, meaning they will always stay within Earth’s orbit. Atens NEAs have a perihelion less than the Earth’s perihelion and a semi-major axis less than one AU. This group is considered “Earth-crossing” since their orbits occasionally cross the Earth’s orbit. Another Earth-crossing category is the Apollo group. These asteroids have a perihelion within the Earth’s aphelion and a semi-major axis of larger than one AU. The asteroid that impacted Chelyabinsk, Russia in 2013 is an example of an Apollo asteroid (Zuluaga et al. 2013) (4); these asteroids occasionally cross Earth’s orbit and are potential candidates for future collisions. The final group of NEAs is the Amor group. These NEAs have an aphelion and perihelion that are more than the Earth’s aphelion and do not cross the Earth’s orbit. These Amor asteroids are also known as Mars-crossing asteroids as they are located between the orbits of Earth and Mars and thus could potentially cross into Mars’ orbit.

The reason NEAs are of such interest is because they have a high potential of colliding with Earth and causing catastrophic damage. Events such as Chelyabinsk and Tunguska, the result of asteroids colliding with Earth, injured thousands of people (Howell, 2019) (Anderson & Whitt 2022) (5) (6). Even more catastrophic was the extinction of the dinosaurs, which was caused by an asteroid 65 million years ago. By tracking NEAs, the potential harm of an asteroid can be gauged and asteroid impact mitigation strategies can be developed. Organizations such as the Center for Near-Earth Object Studies (CNEOS), the European Space Agency (ESA), the Planetary Defense Coordination Office (PDCO), and the Minor Planet Center (MPC) are working to track these asteroids and develop deflection methods should any harm come. However, the monumental task of tracking NEAs has also fallen into the hands of amateur astronomers. By collecting and submitting data from their own observations, knowledge on the orbital paths of both benign and potentially Earth threatening asteroids becomes more robust. As of 2013, there were over 1,400 potentially hazardous NEAs being

tracked (Figure 2), but 10 million Chelyabinsk-sized asteroids (not necessarily NEAs) cross Earth's orbit. As of 2015, only 0.1% of these asteroids (where one hits about every 50 years) (Schweickart 2015) (7) are known and being tracked. While no one was killed during the Chelyabinsk event, the resulting casualties speak to the importance of orbital determination and the tracking of asteroids to provide warnings and time to intervene, mitigate, and deflect.

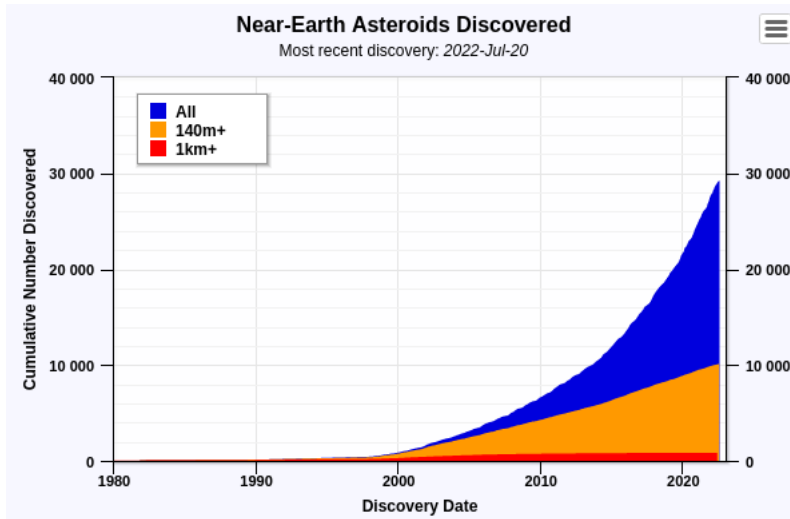


**Figure 2.** Near Earth Asteroids discovered since 1980 (Center for Near Earth Object Studies) (12)

The focus of this team's study throughout Summer Science Program 2022 was 1999 GJ2, an Amor classified NEA. During SSP, 1999 GJ2 had an altitude high enough to be observed at night. The asteroid was also moving at a velocity high enough to allow for the detection of the asteroid's movement between observations, which is necessary for the use of the Method of Gauss.

Asteroids are defined using six main orbital elements (Figure 3). Finding these elements was the ultimate goal of this study, as they are used to determine an ephemeris that determines the position of 1999 GJ2 at any given time. The elements are as follows:

The semi-major axis ( $a$ ) in astronomical units, as calculated in (1.1), is used to measure the size of an asteroid's elliptical orbit. It is half of the distance from the aphelion to the perihelion.  $\mu$  is a

constant that is assumed to be = 1 for this orbital determination.

$$a = \frac{1}{\frac{\frac{r}{2} - \frac{v^2}{\mu}}{r}} \quad (1.1)$$

Eccentricity ( $e$ ), as calculated in (1.2), is the measure of the elongation of an orbital ellipse. As it increases, the orbit is less circular; an eccentricity of 0 is a circle while an eccentricity of 1 is a hyperbola. Eccentricity does not have a unit, as mathematically it is the ratio between the distance between foci and the length of the major axis. For 1999 GJ2, the Sun is at one of the foci of its elliptical orbit.

$$e = \sqrt{1 - \frac{h^2}{a}} \quad (1.2)$$

Inclination ( $i$ ), as calculated in (1.3), is the angle measured between the ecliptic plane and the orbital plane of the asteroid. Inclination ranges from 0 to 180 degrees.

$$i = \cos^{-1} \left( \frac{h_z}{h} \right) \quad (1.3)$$

The ascending node, measured in degrees, is the point where the ecliptic and orbital planes intersect and would result in the asteroid continuing from South to North. The Longitude of Ascending Node ( $\Omega$ ) is the angle between the position of the Vernal Equinox and the ascending node eastward in the ecliptic plane. It ranges from 0 to 360 degrees.

$$\sin(\Omega) = \frac{h_x}{h \sin i} \quad (1.4)$$

$$\cos(\Omega) = \frac{-h_y}{h \sin i} \quad (1.5)$$

Both (1.4) and (1.5) are needed for quadrant correction to calculate Longitude of Ascending Node. The Argument of Perihelion ( $\omega$ ) is the angle (in degrees) between the vernal equinox and the perihelion measured eastward on the orbital plane.

The True Anomaly ( $\nu$ ), the angle from the perihelion to the position vector,  $\vec{r}$ , and  $U$ , the angle between the line of ascending nodes and  $\vec{r}$ , are needed to find the Argument of Perihelion. Both (1.6) and (1.7) are needed for quadrant correction to calculate  $\nu$ , and both (1.8) and (1.9) are needed

for quadrant correction to calculate  $U$ .

$$\cos(\nu) = \frac{1}{e} \cdot \left( \frac{a(1-e^2)}{r} - 1 \right) \quad (1.6)$$

$$\sin(\nu) = \frac{a(1-e^2)}{h \cdot e} \cdot \frac{(r_{vec} \cdot r_{vecdot})}{r} \quad (1.7)$$

$$\sin U = \frac{r_z}{r \cdot \sin i} \quad (1.8)$$

$$\cos U = \frac{x \cdot \cos(\Omega) + y \cdot \sin(\Omega)}{r} \quad (1.9)$$

To ultimately calculate the Argument of Perihelion, (1.10) is used.

$$\Omega = U - \nu \quad (1.10)$$

The final orbital elements are the Mean Anomaly ( $M$ ), as ultimately calculated by (1.13), and Time of Last Perihelion Passage ( $T$ ), calculated inof (1.15). The Mean Anomaly, ranging from 0 to 360 degrees, is where the asteroid would be if it were in a circular orbit as viewed from the center of the ellipse. Time of Perihelion Passage represents the last time the asteroid was at its perihelion in Julian Days.

$$\cos E = \frac{(e + \cos \nu)}{1 + e \cos v} \quad (1.11)$$

$$\sin E = \frac{(r \sin \nu)}{a\sqrt{1-e^2}} \quad (1.12)$$

$$M = E - e \sin E \quad (1.13)$$

$$n = \frac{k}{a^{1.5}} \quad (1.14)$$

$$T = t - \frac{M}{n} \quad (1.15)$$

The method used to determine the orbital elements of 1999 GJ2 was the Method of Gauss. The Method of Gauss is far more accurate for asteroids closer to Earth than using the Method of Laplace, which works well for Main Asteroid Belt asteroids, but not for NEAs. Seeing as 1999 GJ2 is an NEA, the Method of Gauss can be used to determine the orbital elements. This method requires three sets of observations on separate nights that are spaced out in time to allow the asteroid to move a measurable amount between observations. Observation nights had to be clear so clouds would not

block the view of the asteroid. A bright moon would also potentially make observing a relatively dim and higher magnitude asteroid very difficult to image. One final consideration for the nights of observation is that there could not be a bright star near the asteroid. Bright stars would block the asteroid from view in the picture, rendering the observations useless. After obtaining the right ascension and declination of the asteroid using astrometry, the Method of Gauss revolves around making an initial guess of the position and velocity vectors of the asteroid and slowly improving them until they converge, as outlined by the version of the method provided by Boulet (Boulet 2021) (8).

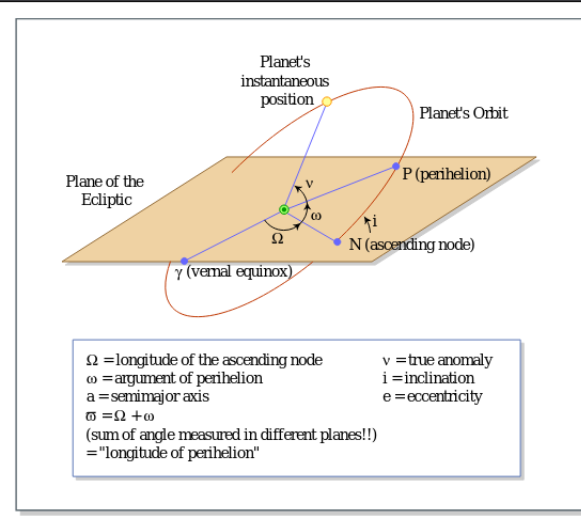


Figure by MIT OCW.

**Figure 3.** Orbital Elements Visualization (Binzel 2006) (13)

## 2. OBSERVATIONS AND IMAGE PROCESSING

### 2.1. Data Acquisition

Data was collected at the University of Colorado, Boulder from the Sommers-Bauch Observatory (code 463). Pictures of 1999 GJ2 were taken using the Artemis East telescope (Figure 6) with a CDK20 Optical Tube Assembly. This 20" PlaneWave reflecting telescope had an aperture f/6.8, a 3454 mm focal length, a 52 x 52 arcminute field of view, and 16,803 size camera sensors. The telescope employed the STF - 8300 camera (Figures 4-5) which utilizes the Kodak KAF - 8300 CMOS. The camera had a 3326 x 2504 pixel array, a 17.96 x 13.52 mm CMOS size, a full well capacity of

25,500  $e^-$ , and 0.37  $e^-/\text{ADU}$  gain. The telescope's primary mirror was 20" in diameter and the secondary mirror was 7.5" in diameter; both were composed of fused silica. The SkyX astronomy and imaging software was used in tandem with the Artemis East telescope. (CloudBreak 2022) (Diffraction Limited 2022) (9) (10)



**Figure 4.** STF 8300 CMOS: Front (10)



**Figure 5.** STF 8300 CMOS: Back(10)

To prepare for each observation, an ephemeris generated by JPL Horizons along with a sky chart was included in the observing notebooks and ultimately used as references during observations. Furthermore, notes were taken in the observing notebooks throughout the imaging process. The date and time of each major event was recorded, including when flat frames were taken, when focusing was completed, and when light series were completed. Additional notes such as the temperature and power of the telescope, the weather and how it changed over the observing period, and other notable events (such as problems with slewing the telescope on June 28th, 2022) were recorded along with their timestamps. A shortened summary of all observations (containing notes from the observing notebook entries) can be found in Table 1.

There are many steps that are needed to take proper pictures of the asteroid. Before every observation, an ephemeris for every fifteen minutes spanning the entire observing period (usually 03:30 - 05:00 UTC) was made using JPL Horizons. After, the data in the ephemeris was put into DS9 to generate a sky chart, or an image of the star field for the expected location of the asteroid in the sky.

At the start of each observation, the set-up procedure was followed; the cover was removed and the telescope was slewed to the flat section of the ceiling to take flat frames. Following this, using an exposure time of two seconds with 2x2 binning and no reduction, five flat frames were taken in order to determine irregularities in the images that would then be removed from the final images during the reduction process. Dark frames, pictures with no exposure to light, were taken with the exact same settings as the flat frames. By taking these, the background brightness could be subtracted from the flat images to create a “master flat” which would be used in image reduction to correct the image. After taking the images needed for the master flat, the cover was put back on the telescope to protect it from dust as the roof opened. The cover was then replaced by the Bahtinov Mask, and the telescope was focused by examining a bright star as a reference. The telescope was slewed to the star Arcturus using the “Find” tool in SkyX. By making slight positional changes while taking a continuous series of 0.2 second exposure time light frames with 2x2 binning and no reduction, the camera was adjusted so that the telescope was in focus. This was achieved when the angles between the lines generated by the Bahtinov Mask were bisected. If the angles were not bisected, the camera position would be lowered or raised.

Finally, the telescope was slewed to the right ascension and declination that was provided by the ephemeris for 1999 GJ2 from JPL Horizons. A test light frame image with 60 seconds exposure time, 2x2 binning, and no reduction was taken to compare to the star chart from DS9 to confirm that the correct field of sky (containing the asteroid) was being imaged. A series of three images with the same settings were then taken and saved for later processing and data reduction. Between light series taken, a series of five dark frame images otherwise with the same settings were taken, as they were later used to remove the background brightness of the light frame images during data reduction. Two more sets of images using the light filter were then taken, each ten minutes after the previous set finished. This was done to make sure movement of the asteroid was visible after data reduction was complete.

Out of the four nights that observations were completed, there were a few errors and technical difficulties. On the night of June 28th, the telescope had not been properly turned off by the group

observing prior, so the slewing mechanism was not working. Because of this, the star Spica was used instead of Arcturus to focus. There were also two nights, July 8th and July 12th, where the telescope had not been set to J2000, a setting which changes the position of right ascension and declination so that the positions of the celestial bodies are given relative to their positions in the year 2000. Because of this, test images needed to be retaken and rechecked against the star chart for confirmation. Finally, the observation for July 8th was rendered mostly useless with the exception of the final series. During image reduction, it was noticed that a star was directly positioned behind the asteroid, making it impossible to tell the location of the asteroid in the night sky due to the inability to properly identify the centroid using aperture photometry.



**Figure 6.** Artemis Telescope on observation deck of Sommers-Bausch Observatory in Boulder, Colorado.

Credit: Alison Soong

Date (UTC)	Time (UTC)	Loc.	Telescope	Filter	Exp. (s)	Weather	Notes
2022-06-28	04:22:01.830	SBO	Artemis	UV/IR	60	Light cloud cover	New Moon
2022-06-28	04:33:44.089	SBO	Artemis	UV/IR	60	Light cloud cover	New Moon
2022-06-28	04:51:15.612	SBO	Artemis	UV/IR	60	Light cloud cover	New Moon
2022-07-08	04:37:39.022	SBO	Artemis	UV/IR	60	Light cloud cover	Asteroid too close to star
2022-07-08	04:38:40.426	SBO	Artemis	UV/IR	60	Light cloud cover	Asteroid too close to star
2022-07-08	04:39:51.830	SBO	Artemis	UV/IR	60	Light cloud cover	Asteroid too close to star
2022-07-08	04:51:23.299	SBO	Artemis	UV/IR	60	Light cloud cover	
2022-07-08	04:13:35.743	SBO	Apollo	UV/IR	60	Light cloud cover	Asteroid too close to star
2022-07-08	04:25:50.329	SBO	Apollo	UV/IR	60	Light cloud cover	Asteroid too close to star
2022-07-08	04:38:40.426	SBO	Apollo	UV/IR	60	Light cloud cover	
2022-07-12	04:04:10.164	SBO	Artemis	UV/IR	60	No cloud cover	98% Full Moon
2022-07-12	04:16:40.826	SBO	Artemis	UV/IR	60	No cloud cover	98% Full Moon
2022-07-12	04:29:21.189	SBO	Artemis	UV/IR	60	No cloud cover	98% Full Moon
2022-07-14	04:31:37.730	SBO	Artemis	UV/IR	60	No cloud cover	99% Full Moon
2022-07-14	04:41:39.025	SBO	Artemis	UV/IR	60	No cloud cover	99% Full Moon
2022-07-14	04:52:23.923	SBO	Artemis	UV/IR	60	No cloud cover	99% Full Moon

**Table 1.** Journal of Observations - Note that every table entry is a series of three images

## 2.2. *Image Reduction*

The AstroImageJ (AIJ) software was used to perform data reduction on the images of 1999 GJ2. After creating master flats and a master dark for the two second exposures of flat and dark images, dark subtraction and flat division was performed on the stack of original light images. Next, the same light image stack was processed again using dark subtraction for a master dark of the sixty second exposure dark frames. The final processed image stack was produced after aligning the reduced image using AIJ's image stabilizer. This data reduction removed instrumental signatures and other possible contaminants which could cause errors in the light images and affect measurements during astrometry and photometry.

To perform astrometry, <https://nova.astrometry.net/> and AIJ was used along with the processed images. After three images from each observation were chosen (usually one image from each light frame series taken), each image was uploaded to nova.astrometry.net, which generated new-image.fits and corr.fits files. The new-image.fits files contained assigned right ascensions and declinations to every pixel in the image, allowing for aperture photometry in AIJ to find the right ascension and declination of 1999 GJ2 based on its centroid in each image (Figure 7). Aperture photometry, SNR (signal to noise ratio) photometry, involves a circle for the aperture (the sum of the pixel values) and two additional concentric circles to the aperture, the outer and inner annulus. All pixels of the asteroid or star in question must fit within the aperture's circle to be included in the total pixel count to aid in accurately calculating the position of the centroid. No other light sources (such as other stars) should appear in the annulus, as the outer annulus is used as a reference for the pixel count of the background, thus excluding these pixels from the final measured pixel count of the object in question. Accessing the FITS header of each new-image.fits provided the precise UTC date and time (to the millisecond) of when each image was taken.

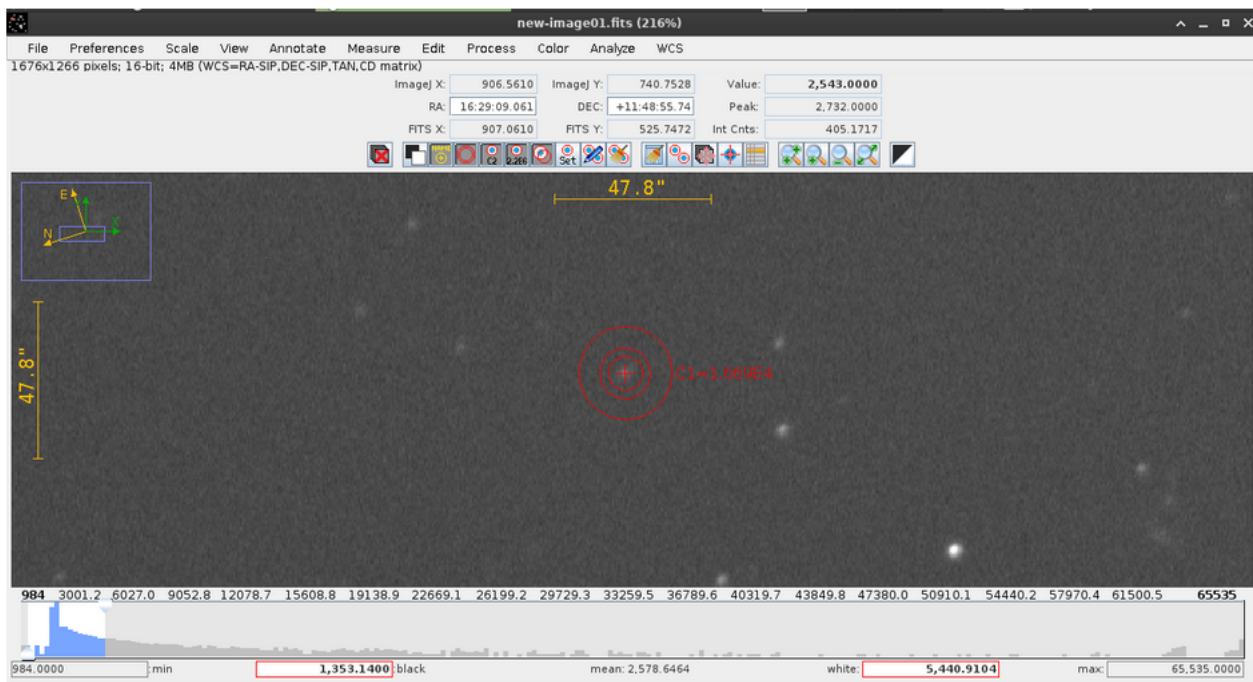


**Figure 7.** Example aperture in AstroImageJ

To perform photometry, the new-image.fits files from nova.astrometry.net, AIJ, and SAOImage DS9 were used. After retrieving the AAVSO Photometric All Sky Survey (APASS) DR9 (designation II/336) in DS9, three reference stars with visual magnitude  $<15$  were selected for each image for a given observation. Using AIJ and aperture photometry, these stars were verified to be unsaturated and information about their pixel counts (source-sky) were found. Due to possible pixel contamination from neighboring stars, which would consequently increase the pixel counts and skew the comparison, another requirement for the three reference stars chosen was to be in close proximity to the asteroid for better comparison but not close to any other stars. The same reasoning applies to the asteroid; the images from July 8th, 2022 were not used in the photometry process since the asteroid passes through a star, which would significantly affect the asteroid's pixel count. For all other images, the asteroid's pixel count was found using aperture photometry in AIJ through a similar process as in astrometry that determined the centroid's right ascension and declination. With the collected data, a linear regression was performed for each image's corresponding three reference stars, with the y-axis taken as the apparent magnitude of each star and the x-axis taken as  $\log_{10}(\text{source} - \text{sky})$  (where source-sky is the pixel counts). Finally, the apparent magnitude of the asteroid was calculated with the line of best fit from the linear regression by plugging in the logarithm (base 10) of the pixel count. This process was repeated for each image in each observation, excluding the observation on July 8th. Table 3 outlines the photometry results from performing linear regressions to calculate 1999 GJ2's apparent magnitude (Vmag) for each suitable image, comparing the calculated values to JPL Horizons' values.

### 2.3. Determination of Errors in Astrometry

To determine the errors in astrometry, the corr.fits files from nova.astrometry.net were used to find each image's error using the root mean square (2.1) of the right ascension and declination uncertainties.

$$RMS = \sqrt{\frac{\sum(x_f - x_i)^2}{N}} \quad (2.1)$$

In equation (2.1),  $x_f - x_i$  is the difference between each field declination/right ascension and its corresponding index declination/right ascension (these values were obtained from the data within the corr.fits file), and N is the number of data points. Each image had one root mean square for right ascension and one root mean square for declination. These root mean squares were critical for later use in the Monte Carlo simulation to generate a random normal distribution in right ascension and declinations. However, they can also be interpreted as the approximate range for the right ascension and declination values from performing astrometry for the asteroid. Table 2 outlines the astrometry results from performing aperture photometry to find 1999 GJ2's position, along with the uncertainty in degrees for both the right ascension and declination values for each image.

#### 2.4. Results

**Table 2.** Astrometry Results

Date (UTC)	Time (UTC)	Julian Date	RA (HMS)	RA Unc. (Deg)	Dec (DMS)	Dec Unc. (Deg)
2022-06-28	04:22:01.830	2459758.6819656	16h29m13.66s	$\pm 5.72563 \times 10^{-5}$	+11d49m48.9s	$\pm 5.52925 \times 10^{-5}$
2022-06-28	04:33:44.089	2459758.6900936	16h29m13.23s	$\pm 5.79348 \times 10^{-5}$	+11d49m50.5s	$\pm 5.58112 \times 10^{-5}$
2022-06-28	04:51:15.612	2459758.7022640	16h29m12.60s	$\pm 1.63587 \times 10^{-4}$	+11d49m52.2s	$\pm 7.04296 \times 10^{-5}$
2022-07-08	04:20:38.188	2459768.6809975	16h23m41.90s	$\pm 3.14938 \times 10^{-5}$	+11d43m21.6s	$\pm 1.49789 \times 10^{-5}$
2022-07-08	04:38:40.426	2459768.6935234	16h23m41.90s	$\pm 3.14160 \times 10^{-5}$	+11d43m21.3s	$\pm 1.18024 \times 10^{-5}$
2022-07-08	04:39:51.830	2459768.6943499	16h23m41.87s	$\pm 3.58318 \times 10^{-5}$	+11d43m21.1s	$\pm 1.63780 \times 10^{-5}$
2022-07-12	04:04:10.164	2459772.6695621	16h22m54.01s	$\pm 2.50364 \times 10^{-5}$	+11d23m27.2s	$\pm 2.95302 \times 10^{-5}$
2022-07-12	04:16:40.826	2459772.6782503	16h22m53.90s	$\pm 2.77597 \times 10^{-5}$	+11d23m23.8s	$\pm 2.97877 \times 10^{-5}$
2022-07-12	04:29:21.189	2459772.6870508	16h22m53.79s	$\pm 2.94814 \times 10^{-5}$	+11d23m20.7s	$\pm 2.68392 \times 10^{-5}$
2022-07-14	04:31:37.730	2459774.6886311	16h22m48.57s	$\pm 1.87851 \times 10^{-5}$	+11d10m04.0s	$\pm 1.41637 \times 10^{-5}$
2022-07-14	04:41:39.025	2459774.6955906	16h22m48.54s	$\pm 1.70018 \times 10^{-5}$	+11d10m00.9s	$\pm 1.42362 \times 10^{-5}$
2022-07-14	04:52:23.923	2459774.7030547	16h22m48.51s	$\pm 1.72357 \times 10^{-5}$	+11d09m57.4s	$\pm 1.58472 \times 10^{-5}$

**Table 3.** Photometry Results

Date (UTC) and Observation	Calculated Asteroid Vmag	Asteroid JPL Vmag	% Difference
6/28/2022 (Obs 1)	17.754	17.490	1.511%
6/28/2022 (Obs 2)	17.506	17.490	0.091%
6/28/2022 (Obs 3)	17.605	17.490	0.658%
7/12/2022 (Obs 1)	17.623	17.700	0.433%
7/12/2022 (Obs 2)	17.672	17.700	0.161%
7/12/2022 (Obs 3)	17.835	17.700	0.761%
7/14/2022 (Obs 1)	17.919	17.700	1.238%
7/14/2022 (Obs 2)	17.840	17.700	0.793%
7/14/2022 (Obs 3)	17.631	17.700	0.392%

### 3. ORBIT DETERMINATION

#### 3.1. *Methods*

Orbital determination was performed through a Python program written that implemented the Method of Gauss. The Method of Gauss calculates an asteroid's position and velocity vector of the central observation by picking an initial guess for the central observation vectors, then iterating until those vectors converge. The Method of Gauss needs data for three observations. The critical relation that the Method of Gauss depends on is in Figure 8.

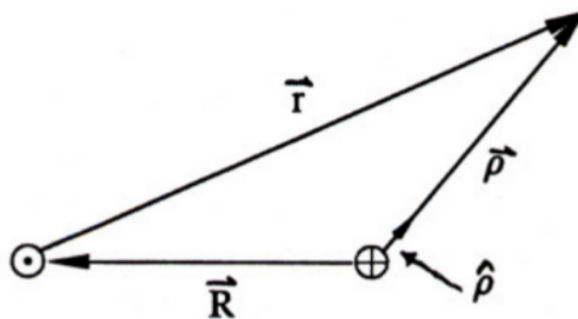


**Figure 8.**  $\vec{r} = \rho\hat{\rho} - \vec{R}$  (Boulet 2021) (8)

In Figure 8,  $\vec{r}$  is the asteroid's position vector from the Sun,  $\rho$  is the magnitude of the asteroid's position vector from Earth,  $\hat{\rho}$  is the direction of the asteroid from Earth, and  $\vec{R}$  is the position vector from the Earth to the Sun (Figure 8). By calculating the position and velocity vector it is then possible to calculate an asteroid's orbital elements

The first step within the orbital determination was obtaining an initial guess for  $\vec{r}$  and  $\vec{r}_2$  by inputting the observation times ( $t$  in Julian Days), right ascensions ( $\alpha$ ), declinations ( $\delta$ ), and Sun distance vectors ( $\vec{R}$ ) in AU and the equatorial plane of 1999 GJ2 into the Method of Gauss for three observations. Data from June 28th, July 12th, and July 14th was used as input for the Method of Gauss, as July 8th only had a single viable series to use for astrometry due to the presence of a star directly next to the asteroid. After inputting observation data,  $\hat{\rho}$ s were found (3.1).

$$\hat{\rho}_i = \cos\alpha_i \cos\delta_i \hat{i} + \sin\alpha_i \cos\delta_i \hat{j} + \sin\delta_i \hat{k} \quad (3.1)$$

where  $\hat{\rho}_i$  was the  $\hat{\rho}_i$  vector for a specific observation,  $\alpha_i$  was the right ascension for a specific observation, and  $\delta_i$  was the declination for a specific observation.

These  $\hat{\rho}$  vectors were then used to determine the ten D coefficients (3.2-3.5).

$$D_0 = \hat{\rho}_1 \cdot (\hat{\rho}_2 \times \hat{\rho}_3) \quad (3.2)$$

$$D_{1j} = (\vec{R}_j \times \hat{\rho}_2) \cdot \hat{\rho}_3 \quad (3.3)$$

$$D_{2j} = (\hat{\rho}_1 \times \vec{R}_j) \cdot \hat{\rho}_3 \quad (3.4)$$

$$D_{3j} = \hat{\rho}_1 \cdot (\hat{\rho}_2 \times \vec{R}_j) \quad (3.5)$$

where,  $j = 1, 2, 3$  for a respective observation. Using the  $ts$ , the  $\tau$  (time differences between observations) were also calculated (3.6-3.8).

$$\tau_1 = k(t_1 - t_2) \quad (3.6)$$

$$\tau_3 = k(t_3 - t_2) \quad (3.7)$$

$$\tau = \tau_3 - \tau_1 \quad (3.8)$$

With the now calculated  $\hat{\rho}_2$ ,  $\tau$ s, and the previously known  $\vec{R}_2$  which was inputted into the Method of Gauss, potential guesses for the magnitudes of  $\vec{r}_2$  and  $\vec{\rho}_2$  were found using the Scalar Equation of

Lagrange (SEL) (3.9), an 8th order polynomial

$$r_2^8 + ar_2^6 + br_2^3 + c = 0 \quad (3.9)$$

where,  $a$ ,  $b$ , and  $c$ , are all coefficients dependent on the  $\tau$ s and  $D$  coefficients.

Multiple roots for the SEL were possible, so the  $r_2$  magnitude used to continue the Method of Gauss had to be chosen carefully such that it was positive, real, and had a corresponding positive and real  $\rho_2$  value.

$r_2$  and the  $\tau$ s were then used to calculate a new set of coefficients,  $f_1, f_3, g_1$ , and  $g_3$ . These coefficients were defined by a Taylor series. For obtaining the initial guess, only the second degree Taylor Series was used since higher degrees are dependent on  $\vec{r}_2$  and  $\dot{\vec{r}}_2$  (3.10-3.11).

$$f_i = 1 - \frac{\mu}{2r_2^3} \tau_i^2 + \frac{\mu(\vec{r}_2 \cdot \dot{\vec{r}}_2)}{2r_2^3} \tau_i^3 + \dots \quad (3.10)$$

$$g_i = \tau_i - \frac{\mu}{6r_2^3} \tau_i^3 + \dots \quad (3.11)$$

Here,  $\mu$  was a constant,  $\mu \approx GM_{\odot}$ , and  $i$  was the specific observation. The next step after obtaining the  $f$  and  $g$  coefficients was to calculate  $C$  coefficients for each observation (3.12-3.14).

$$C_1 = \frac{g_3}{f_1 g_3 - g_1 f_3} \quad (3.12)$$

$$C_2 = -1 \quad (3.13)$$

$$C_3 = \frac{-g_1}{f_1 g_3 - g_1 f_3} \quad (3.14)$$

Using the  $C$  and  $D$  coefficients, the magnitudes of the  $\vec{\rho}$ 's were found (3.15)

$$\rho_i = \frac{C_1 D_{i1} + C_2 D_{i2} + C_3 D_{i3}}{C_i D_0} \quad (3.15)$$

where  $i$  is the corresponding values for each specific observation. Since both the unit vectors  $\hat{\rho}$  and magnitudes  $\rho$  were now known for each observation,  $\vec{\rho}$  vectors were calculated by dotting  $\hat{\rho} \cdot \rho$ . Since the  $\vec{\rho}$  vectors were now known,  $\vec{r} = \rho \hat{\rho} - \vec{R}$  from Figure 8 was used to find the  $\vec{r}$  position vector for each observation.  $\dot{\vec{r}}_2$  was then calculated using already known information (3.16).

$$\dot{\vec{r}}_2 = \frac{f_3}{f_3 g_1 + f_1 g_3} \vec{r}_1 + \frac{f_1}{f_1 g_3 - f_3 g_1} \vec{r}_3 \quad (3.16)$$

This resulted in the initial guess for  $\vec{r}_2$  and  $\dot{\vec{r}}_2$ . These initial guesses were then made more precise by iterating through these equations once again using a higher order Taylor series for  $f$  and  $g$  until  $\vec{r}_2$  and  $\dot{\vec{r}}_2$  converged.

An important thing to note is that the observation times needed to be corrected for light-travel time to iterate. The observation times that were inputted originally into the Method of Gauss corresponded to the time that the light hit the telescope, not when it left the asteroid. Inner solar system objects have light-travel times in the order of minutes, so light-travel time correction is necessary. The observation times can be corrected by (3.17).

$$t_{corrected} = t_i - \frac{\rho_i}{c} \quad (3.17)$$

In (3.17),  $c$  is the speed of light in AU/(mean solar) day. After the final  $\vec{r}_2$  and  $\dot{\vec{r}}_2$  were calculated, the orbital elements were calculated using equations 1.1-1.15.

After obtaining the orbital elements for 1999 GJ2, a self-consistency test was performed by predicting the location of the asteroid for the third observation (July 14, 2022) by generating an ephemeris. The calculated right ascension and declination was then compared with the measured right Ascension and declination. Refer to Table 4 for the results of the self-consistency test.

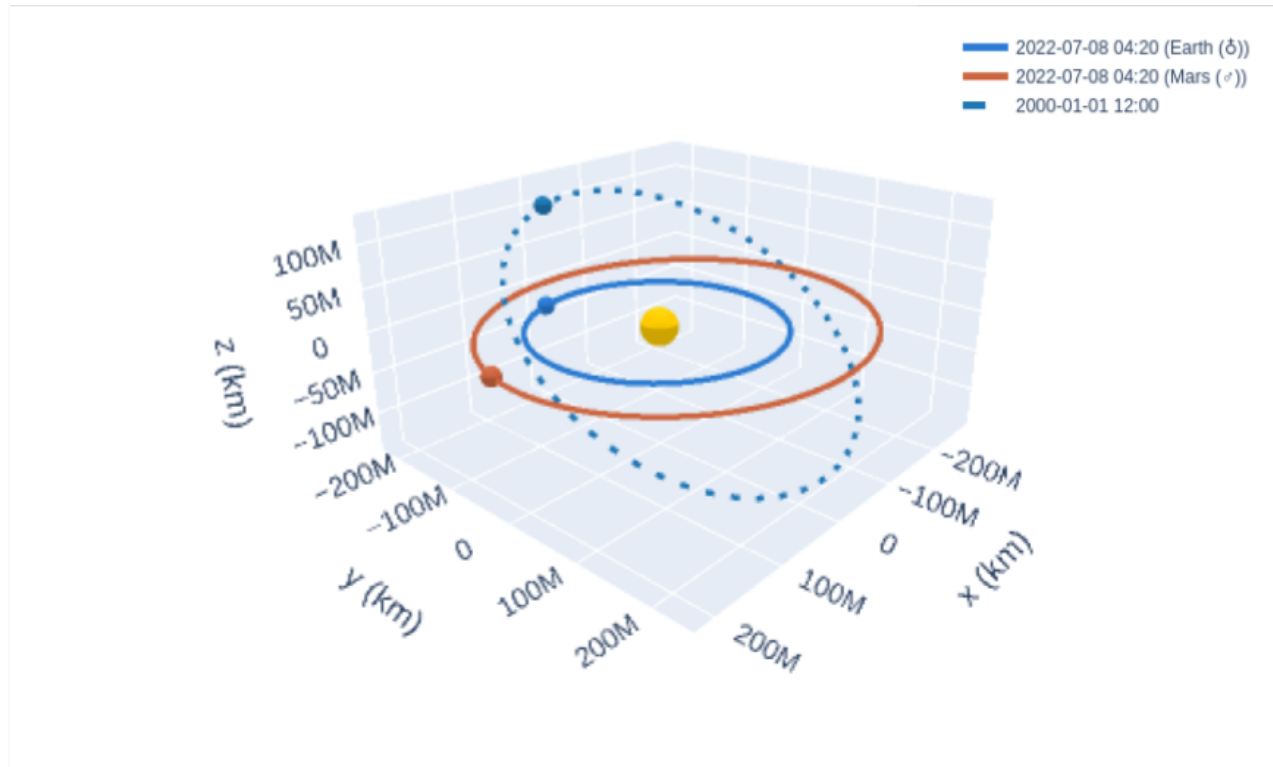
There were many uncertainties involved in the measurement of 1999 GJ2 such as uncertainty in CMOS imaging and centroid determination due to possible software imprecision. Furthermore, the Method of Gauss does not account for possible perturbations in 1999 GJ2's orbit from other solar system bodies. Due to this, Monte Carlo Simulation was used to determine final values and uncertainties in the orbital elements. A normal distribution was assumed for both right ascension and declination, and using the previously determined errors from each corr.fits file (as described Section 2.3),  $n = 100,000$  random samples were taken from the normal distribution. Using each new right ascension and declination, the Method of Gauss was rerun and randomly sampled distributions for each orbital element were produced. The mean and standard deviation of these randomly sampled distributions were then used as the final value and uncertainty for each orbital element of 1999 GJ2 and each distribution was plotted as a histogram (Figures 10-16).

Date	2022 – 07 – 14
Time (UTC)	04 : 41 : 39.025
Calc. RA (Deg)	16 : 22 : 48.54604
Astrometry RA (Deg)	16 : 22 : 48.54
% Error RA	$1.02446 \times 10^{-5}$
Astrometry Dec (Deg)	11 : 10 : 0.92715
Calc. Dec (Deg)	11 : 10 : 0.9
% Error Dec	$6.75249 \times 10^{-5}$

**Table 4.** Self-consistency Test

Using these calculated orbital elements, a visualization of 1999 GJ2’s orbit was made using the poliastro package (Figure 9). For more information about orbital determination or for access to the orbital determination code, contact the authors of this paper.

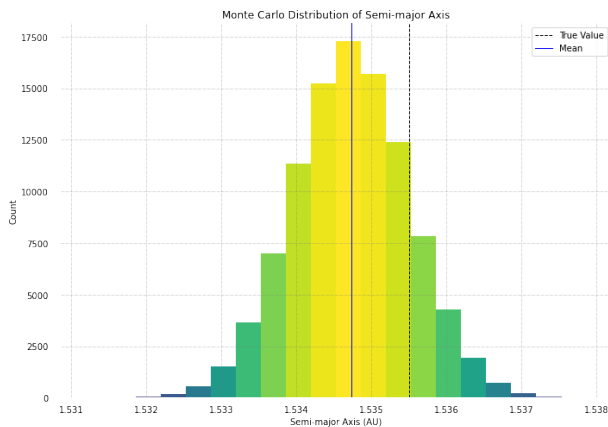
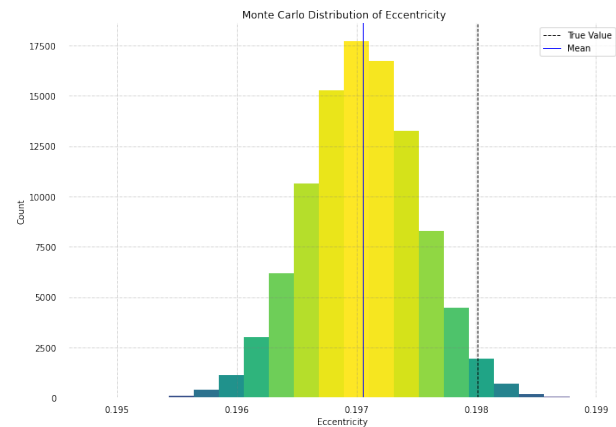
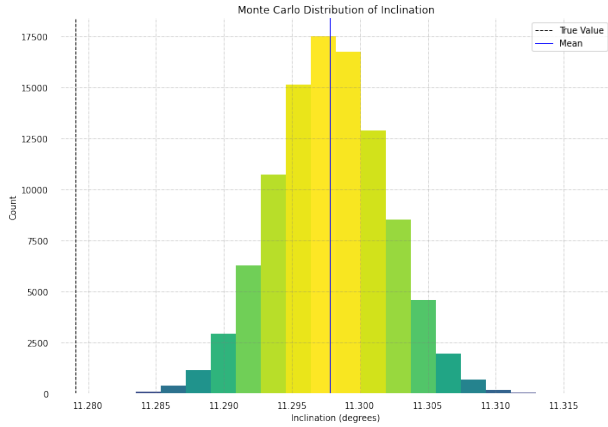
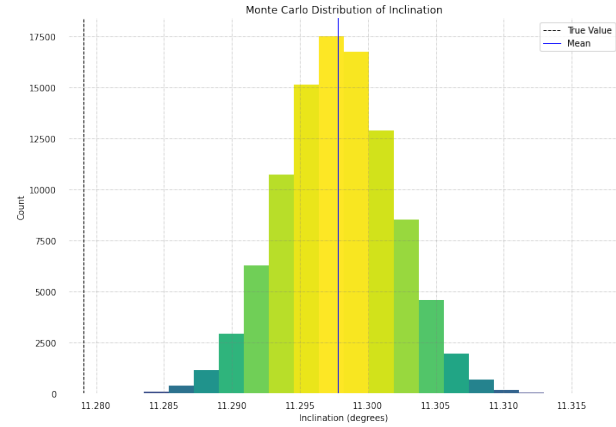
### 3.2. Results



**Figure 9.** 3D Visualization of 1999 GJ2's Orbit

**Table 5.** Calculated Orbital Elements

Orbital Element	Mean	Standard Deviation (unc.)	Actual JPL Values	% Diff from JPL
Semi-Major Axis (AU)	1.53473	$7.73128 \times 10^{-4}$	1.53550	$4.99834 \times 10^{-2}$
Eccentricity	0.19705	$4.66379 \times 10^{-4}$	0.19801	$4.84841 \times 10^{-1}$
Inclination (Deg)	11.29781	$4.13283 \times 10^{-3}$	11.27908	$1.66043 \times 10^{-1}$
Longitude of Ascending Node (Deg)	196.30890	$4.51323 \times 10^{-2}$	196.19763	$5.67112 \times 10^{-2}$
Argument of Perihelion (Deg)	142.49775	$4.81499 \times 10^{-3}$	142.53255	$2.44164 \times 10^{-2}$
Mean Anomaly (Deg)	316.23192	$7.76157 \times 10^{-2}$	316.39376	$5.11518 \times 10^{-2}$
Time of Perihelion Passage (JD)	2459162.64815	$6.07527 \times 10^{-1}$	2459856.85988	$3.13276 \times 10^{-5}$

**Figure 10.** Monte Carlo Distribution of Semi-major Axis**Figure 12.** Monte Carlo Distribution of Eccentricity**Figure 11.** Monte Carlo Distribution of Inclination**Figure 13.** Monte Carlo Distribution of Inclination

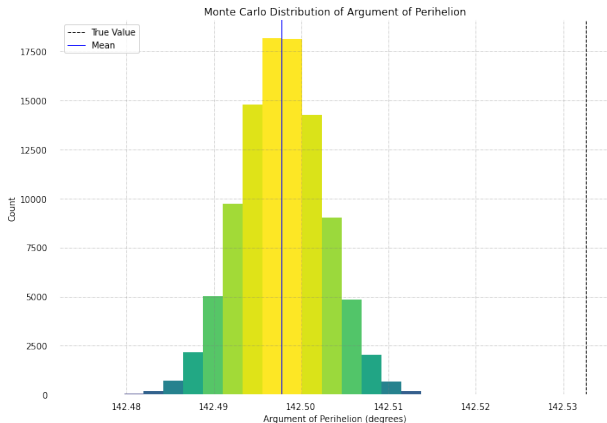


**Figure 14.** Monte Carlo Distribution of Argument of Perihelion

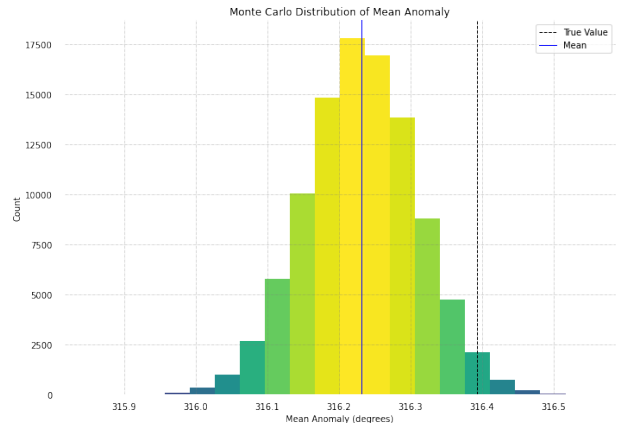


**Figure 15.** Monte Carlo Distribution of Mean Anomaly

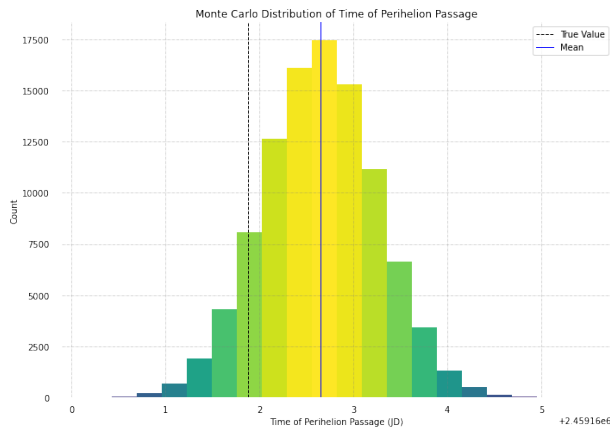


**Figure 16.** Monte Carlo Distribution of Time of Perihelion Passage

#### 4. DISCUSSION

All of the percent errors comparing the calculated orbital determination data compared to the accepted JPL data are less than 1%. Although there is error (albeit very small) between the calculated data to JPL Horizons', it is not possible to know for certain which set of values describes the actual orbit of 1999 GJ2 more precisely. When the calculated orbital elements are inputted into an ephemeris to generate the position of the asteroid for July 12th, 2022 at 04 : 41 : 39.025 UTC , the resulting right ascension and declination are precise to less than an arcsecond. This self-consistency test (Table

4) illustrates that the final orbital determination reflects the obtained data throughout this study with minimal error.

It is important to note that when determining the error between calculated values from the orbital determination code and accepted values from JPL Horizons, JPL Horizons gave a value that did not match the calculated Time of Perihelion Passage. Instead, the difference between calculated and accepted value was some multiple of the asteroid's period, meaning JPL Horizons' value was not necessarily the closest (in the same orbit) as the middle, or second, observation time used for orbital determination. Therefore, the calculated time of perihelion was ultimately compared to an adjusted value. To find the period of the asteroid, Kepler's Third Law,  $T^2 = a^3$ , was used since the period is calculated in Gaussian days. Units were corrected by multiplying by  $G_d$ , the number of Gaussian days in a year (365.2568983 days/year). Thus the period was found to be

$$T_{\text{period}} = G_d a^{3/2} \quad (4.1)$$

where  $a$  is the accepted value for the asteroid's semi-major axis. To adjust JPL Horizon's time of perihelion value, the following formula was used:

$$T_a = t_2 - \text{mod}(t_2 - T, T_{\text{period}}) \quad (4.2)$$

where  $T_a$  is the final adjusted Time of Perihelion Passage,  $t_2$  is the time of the middle observation in Julian days,  $T$  is the original Time of Perihelion from JPL Horizons, and  $T_{\text{period}}$  is the calculated period of the asteroid using JPL Horizons' data. This minimized the percent error for the Time of Perihelion to  $3.13 \times 10^{-5}\%$ , which roughly corresponds to a difference of 1 JD between the calculated root mean square and the value from JPL Horizons.

Other sources of error were also present in the orbital determination. Floating-point imprecision in Python resulted in the calculations being rounded to a limit of sixteen decimals. Due to this imprecision, error propagation occurred in all calculations performed.

Another factor affecting the quality of results was the precision of constants used. The code used constants  $k$  (gravitational constant in AU),  $\epsilon$  (tilt of the Earth's axis in degrees), and  $c$  (the speed of light in AU), all of which were rounded to a specific number of significant figures. Another similar factor arises with the observation data itself. The right ascension and declination from the photometry of the asteroid were only precise to four and three significant figures, respectively.

One final factor affecting the result quality was conversion to Julian Day time. The JPL Horizons JD Date/Time Converted was used to convert the UTC time into Julian Days. The precision of this conversion was limited by the calculations performed by JPL Horizons. All of these imprecision factors together contributed to error. In short, the orbital determination was limited by data and calculation precision.

Furthermore, uncertainty regarding the precision of CMOS imaging and centroid determination along with the limitations of the Method of Gauss for accounting for multiple solar system bodies as described in Section 3.1 also contributed to error and the quality of the orbital determination results.

If a library such as mpmath was used for calculations instead of numpy and math, the float imprecision could be diminished since more significant figures could be used. This would increase precision of the final results.

Earth is also processing along its axis, so the value of the tilt of Earth's axis is different each day. This was not accounted for in the  $\epsilon$  constant used. If the value for  $\epsilon$  was adjusted for each day instead of using a constant, the precision of data would be increased.

Differential correction could also have been used to improve the accuracy of the data. The propagating uncorrelated errors are like steps in a random walk; the error produced from the data points can be calculated using the root mean square of the individual uncorrelated errors and can be accounted for. In summary, the data could be improved by increasing precision throughout the entirety of the method.

## 5. REFLECTION

Our overall experience completing this project was extremely positive; our team collaborated extremely well together, and we all gained extensive knowledge on how to properly conduct scientific

research, from proposing a plan, to field work, and to writing a final paper. Throughout SSP, we used Google Drive, Overleaf, and pdoc docstrings to effectively and efficiently collaborate on our project.

The division of labor between our team was equal. Everyone had working orbital determination code, which outputted data that could have been used as well. Although we only used one team member's final results, the values that the rest of the team obtained all supported and reflected the values used in this report. Everyone contributed to writing, editing, and converting our orbital determination report to L<sup>A</sup>T<sub>E</sub>X. Everyone processed at least one image during the astrometry and photometry process, and everyone got the chance to drive the telescope and take notes. This distribution of work not only enabled us to successfully track our asteroid, but also enabled us to learn the entire research and orbital determination process from start to finish.

While individuals did have strengths and weaknesses, we completely covered each required skill between everyone on the team. We would always see each other working hard, and we always kept each other accountable for our work. As a team, we wished we had gotten a fourth observation. While we observed our asteroid four times, we didn't realize that one of them was inviable for study until after our allotted observation period. We also wish we had started work on the OD report earlier, as we would have liked to try the differential correction for the orbital determination code.

## 6. ACKNOWLEDGEMENTS

Thank you, Dr. Michael Dubson and Dr. Donovan Domingue, for spending numerous hours teaching us everything from the ground up that we needed to know to accomplish our final research project. Thank you to all the TAs, Peter Lande, Jessica Dong, Mia Liang, and Grace Edwards, for your continuous support and guidance late into the night, and for bringing such a positive energy to the observation deck. Thank you, Ms. Kelly Doyle, for your enthusiasm and for always looking out for our well-being as we worked, stumbled, and grew throughout this difficult project. And to all our SSP colleagues, thank you for always being available to answer questions and for making SSP the greatest summer experience of a lifetime.

## REFERENCES

- [1][Barnett, A. 2019, Comets, NASA,  
<https://solarsystem.nasa.gov/asteroids-comets-and-meteors/comets/in-depth/>]
- [2][Barnett, A. 2021, Asteroids, NASA,  
<https://solarsystem.nasa.gov/asteroids-comets-and-meteors/asteroids/in-depth/>]
- [3][NASA JPL CNEOS, 2022, Discovery Statsitics, NASA, <https://cneos.jpl.nasa.gov/stats/>]
- [4][Zuluaga, I. J., Ferrin, I., Geens, S. 2013, The orbit of the Chelyabinsk event impactor as reconstructed from amateur and public footage, arxiv,  
<https://doi.org/10.48550/arXiv.1303.1796>]
- [5][Howell, E. 2019, Chelyabinsk Meteor: A Wake-Up Call for Earth, Space.com,  
<https://www.space.com/33623-chelyabinsk-meteor-wake-up-call-for-earth.html>]
- [6][Anderson, P. S., Whitt, K. K., 2022, The Tunguska explosion, 114 years ago today, EarthSky, <https://earthsky.org/space/what-is-the-tunguska-explosion/>]
- [7][Schweickart, R. 2015, Asteroids 101: What are Asteroids and Where Are They?, B612,  
<https://b612foundation.org/asteroids-101-what-are-asteroids-and-where-are-they-rusty-schweickart-2/>]
- [8][Boulet, 2022, Orbit Determination Packet]
- [9][2022, CDK20 Optical Tube Assembly, CloudBreak (F/6.8),  
<https://cloudbreakoptics.com/collections/telescopes-by-planewave/products/cdk20-optical-tube-assembly-f-6-8>]
- [10][2022, STF-8300, Diffraction Limited/SBIG,  
[https://diffractionlimited.com/wp-content/uploads/2018/06/AAS\\_STF.pdf](https://diffractionlimited.com/wp-content/uploads/2018/06/AAS_STF.pdf)]
- [11][Biktimirov, 2019, Illustration of the four main Near-Earth asteroid groups according to their orbits and compared with the Sun, Earth's and Mars' orbits and the Asteroid Belt, Research Gate,  
[https://www.researchgate.net/figure/Illustration-of-the-four-main-Near-Earth-asteroid-groups-according-to-their-orbits-and\\_fig3\\_336899160](https://www.researchgate.net/figure/Illustration-of-the-four-main-Near-Earth-asteroid-groups-according-to-their-orbits-and_fig3_336899160)]
- [12][Center for Near Earth Object Studies, 2022, Discovery Statistics, JPL/NASA  
<https://cneos.jpl.nasa.gov/stats/totals.html>]
- [13][Binzel, R. 2006, Orbital Elements, MIT Courseware,  
<https://ocw.mit.edu/courses/12-400-the-solar-system-spring-2006/resources/orbitalelements/>]